IEEE Access
Multidisciplinary ⋮ Rapid Review ⋮ Open Access Journal

Received October 26, 2019, accepted November 30, 2019, date of publication December 12, 2019, date of current version December 23, 2019.

Digital Object Identifier 10.1109/ACCESS.2019.2958985

Extended Blind End-Member and Abundance Extraction for Biomedical Imaging Applications

DANIEL U. CAMPOS-DELGADO[1], (Senior Member, IEEE), OMAR GUTIERREZ-NAVARRO[2], JOSE J. RICO-JIMENEZ[3], ELVIS DURAN-SIERRA[3], HIMAR FABELO[4], SAMUEL ORTEGA[4], GUSTAVO CALLICÓ[4], (Member, IEEE), AND JAVIER A. JO[3,5]

[1]Faculty of Sciences, Universidad Autónoma de San Luis Potosí, San Luis Potosí 78295, México
[2]Biomedical Engineering Department, Universidad Autónoma de Aguascalientes, Aguascalientes 20340, México
[3]Department of Biomedical Engineering, Texas A&M University, College Station, TX 77843, USA
[4]Institute for Applied Microelectronics, University of Las Palmas de Gran Canaria, 35017 Las Palmas de Gran Canaria, Spain
[5]School of Electrical and Computer Engineering, The University of Oklahoma, Norman, OK 73019, USA

Corresponding author: Daniel U. Campos-Delgado (ducd@fciencias.uaslp.mx)

This work was supported in part by the Basic Science Grant of CONACYT under Grant 254637, in part by the National Institute of Health under Grant R01CA218739 and Grant R01CA200399, and in part by the Canary Islands Government through the Canarian Agency for Research, Innovation, and the Information Society (ACIISI), ITHACA Project Hyperspectral Identification of Brain Tumors under Grant ProID2017010164.

ABSTRACT In some applications of biomedical imaging, a linear mixture model can represent the constitutive elements (end-members) and their contributions (abundances) per pixel of the image. In this work, the extended blind end-member and abundance extraction (EBEAE) methodology is mathematically formulated to address the blind linear unmixing (BLU) problem subject to positivity constraints in optical measurements. The EBEAE algorithm is based on a constrained quadratic optimization and an alternated least-squares strategy to jointly estimate end-members and their abundances. In our proposal, a local approach is used to estimate the abundances of each end-member by maximizing their entropy, and a global technique is adopted to iteratively identify the end-members by reducing the similarity among them. All the cost functions are normalized, and four initialization approaches are suggested for the end-members matrix. Synthetic datasets are used first for the EBEAE validation at different noise types and levels, and its performance is compared to state-of-the-art algorithms in BLU. In a second stage, three experimental biomedical imaging applications are addressed with EBEAE: m-FLIM for chemometric analysis in oral cavity samples, OCT for macrophages identification in post-mortem artery samples, and hyper-spectral images for *in-vivo* brain tissue classification and tumor identification. In our evaluations, EBEAE was able to provide a quantitative analysis of the samples with none or minimal a priori information.

INDEX TERMS Blind linear unmixing, constrained optimization, fluorescence lifetime imaging microscopy, hyperspectral imaging, optical coherence tomography.

I. INTRODUCTION

For many biomedical applications, the measurements in the dataset can be modeled by a linear combination of some basic components [1]–[4]. These studied measurements could be related to temporal-dynamic responses, spectroscopic and/or morphological information. In particular, this study is concern with measurements that have just non-negative elements, for example related to the intensity of optical characteristics, or spectroscopic information [5]–[9]. The temporal, spectral and/or morphological profiles of the basic components are referred as *end-members*, and their concentrations in the measurements are denoted as the *abundances*. An unmixing analysis allows a quantitative characterization of a dataset by identifying the end-members and their corresponding abundances in a linear mixture model [1]–[3]. Hence, the problem of jointly estimating the end-members and their abundances in a dataset is called blind linear unmixing (BLU) analysis [10]–[12]. The unmixed dataset characterizes the constitutive components of the sample by classifying the end-members, and highlights a quantitative study of their contributions by the abundances [3]. Furthermore, if the measurements in the dataset can be arranged with some spatial information, the estimated abundances can provide

The associate editor coordinating the review of this manuscript and approving it for publication was Gina Tourassi.

concentration maps of the end-members, or even guide a segmentation scheme.

There are standard algorithms in the literature for BLU, for example assuming end-members with linear and/or geometric properties, such as principal component analysis (PCA) or independent component analysis (ICA) [13]–[15]. However, classical ICA and PCA do not consider a non-negativity condition on the resulting end-members, so the estimated vectors might not have a physical interpretation. In this sense, for the unmixing of non-negative datasets, non-negative matrix factorization (NNMF) [16], [17], sparse non-negative matrix factorization (S-NNMF) [18], non-smooth non-negative matrix factorization (NS-NNMF) [19], independent component estimation (ICE) [20], and multi-variate curve resolution (MCR) [21], [22] are popular methodologies. Nonetheless, to our knowledge, blind end-member and abundance extraction (BEAE) is the only available computational tool [3], which estimates non-negative end-members and abundances, plus the abundances are normalized to sum-to-one in each measurement (*probabilistic interpretation*), and the end-members are also normalized in the dataset. One important limitation of BEAE is its scaling property, since the hyper-parameters in the methodology have to be tuned based on the dataset size, as well as the order of the linear mixture model. Furthermore, BEAE was focused just on multi-spectral fluorescence lifetime imaging (m-FLIM). Finally, in [3], the initialization of the end-members matrix in BEAE was discussed as a crucial step, but this condition was not explored further.

In this context, this contribution presents an extension to our early work in [3] that overcomes the original limitations of BEAE, where the new methodology is denoted as extended blind end-member and abundance extraction (EBEAE) methodology, and we demonstrate its application to three different biomedical imaging modalities. Thus, we first introduce the mathematical formulation of EBEAE, and describe the estimation scheme based on constrained quadratic optimization (CQO) and alternated least-squares (ALS) strategies. We adopt a local approach to estimate the abundances of each measurement by maximizing their entropy, and a global technique to identify the end-members. All the quadratic cost functions are normalized to avoid the dependence on the dataset size, and four initialization approaches are suggested for the initial end-members matrix in the iterative scheme. The performance of EBEAE was first analyzed in detail for synthetic datasets at different noise types and levels, and compared to two standard state-of-the-art BLU algorithms: S-NNMF and NS-NNMF [18], [19]. Three biomedical optical imaging applications are analyzed experimentally: multi-spectral fluorescence lifetime imaging (m-FLIM) for chemometric analysis in oral cavity samples, optical coherence tomography (OCT) for macrophages identification in post-mortem artery samples, and hyper-spectral imaging (HSI) for *in-vivo* brain tissue classification and tumor identification.

The notation employed in this work is described next. Scalars, vectors and matrices are denoted by italic, boldface lower-case, and boldface upper-case letters, respectively. A L-dimensional vector with unitary entries and the corresponding identity matrix are defined as $\mathbf{1}_L$, and $\mathbf{I}_L$, respectively. For a vector $\mathbf{x}$, its transpose is represented by $\mathbf{x}^\top$, its l-th component by $(\mathbf{x})_l$, its Euclidean norm by $\|\mathbf{x}\| = \sqrt{\sum_l (\mathbf{x})_l^2}$, and $|\mathbf{x}|$ stands for a new vector obtained by applying the absolute value per component. For a matrix $\mathbf{X}$, $\|\mathbf{X}\|_F = \sqrt{\mathrm{Tr}(\mathbf{X}\mathbf{X}^\top)}$ denotes its Frobenius norm, where $\mathrm{Tr}(\cdot)$ expresses the trace operation; and $\mathrm{rank}(\mathbf{X})$ the maximum number of linearly independent columns in $\mathbf{X}$. A diagonal matrix with elements in the vector $\mathbf{x}$ is defined as $\mathrm{diag}(\mathbf{x})$, and for a symmetric matrix $\mathbf{X}$, $\lambda_{min}(\mathbf{X})$ represents its minimum eigenvalue. For a set $\mathcal{X}$, $\mathrm{card}(\mathcal{X})$ denotes its cardinality, i.e. the number of elements in the set. A vector $\mathbf{x}$ with independent and identically distributed (i.i.d.) Gaussian entries (zero mean and variance σ^2) is denoted as $\mathbf{x} \sim \mathcal{N}(\mathbf{0}, \sigma^2\mathbf{I})$.

The rest of the paper is organized as follows First, Section II presents the BLU formulation, the EBEAE synthesis problem and the proposed design methodology. Next, Section III shows the results obtained in the evaluation of synthetic datasets, and by using three different experimental biomedical imaging use cases. Finally, Section IV exposes the main conclusions achieved during the development of this work.

II. METHODOLOGY

A general framework is considered in this work, where there are assumed K spatial measurements of a physical variable in the dataset. These measurements are expressed as L-dimensional real vectors $\mathbf{z}_k$ with positive entries, i.e.

$$\mathbf{z}_k \in \mathbb{R}^L \quad \forall k \in [1, K] \tag{1}$$

where $\mathbf{z}_k \geq 0$ (i.e. the inequality is interpreted component-wise). Next, without loss of generality, all the measurements $\mathcal{Z} = \{\mathbf{z}_1, \ldots, \mathbf{z}_K\}$ are scaled to sum-to-one

$$\mathbf{y}_k \triangleq \frac{1}{s_k}\mathbf{z}_k \quad \& \quad s_k \triangleq \mathbf{1}_L^\top \mathbf{z}_k, \tag{2}$$

for numerical stability and to restrict the search space. All the selected measurements in $\mathcal{Z}$ need to satisfy a threshold on the acquisition signal-to-noise property, since otherwise the scaling in (2) could enhance the noise contribution and misguide the BLU methodology. The scaled measurements in $\mathcal{Y} = \{\mathbf{y}_1, \ldots, \mathbf{y}_K\}$ are assumed to be represented by a N-th order linear mixture model ($N \geq 2$ and $N < L$):

$$\begin{aligned} \mathbf{y}_k &= \sum_{n=1}^{N} \alpha_{k,n}\mathbf{p}_n + \mathbf{v}_k \qquad \forall k \in [1, K] \\ &= \underbrace{\begin{bmatrix}\mathbf{p}_1 & \cdots & \mathbf{p}_N\end{bmatrix}}_{\mathbf{P}\in\mathbb{R}^{L\times N}} \underbrace{\begin{bmatrix}\alpha_{k,1}\\ \vdots \\ \alpha_{k,N}\end{bmatrix}}_{\boldsymbol{\alpha}_k\in\mathbb{R}^N} + \mathbf{v}_k = \mathbf{P}\,\boldsymbol{\alpha}_k + \mathbf{v}_k \end{aligned} \tag{3}$$

where $\mathbf{p}_n \in \mathbb{R}^L$ is the n-th end-member ($\mathbf{p}_n \geq 0$), $\alpha_{k,n} \geq 0$ its abundance in the k-th measurement, and $\mathbf{v}_k \in \mathbb{R}^L$ is an uncertainty/noise vector. The elements in $\mathbf{v}_k$ are assumed zero-mean and i.i.d. with a Gaussian distribution. In our formulation, we assume that the set of end-members $\mathcal{P} = \{\mathbf{p}_1, \ldots, \mathbf{p}_N\}$ is linearly independent, i.e. rank($\mathbf{P}$) $= N$. Hence each end-member in $\mathcal{P}$ represents a distinctive temporal, spectral and/or morphological profiles in our dataset $\mathcal{Y}$; otherwise the dependent end-members are redundant and should be removed from $\mathcal{P}$. The abundances at any spatial location are normalized to sum-to-one

$$\mathbf{1}_N^\top \boldsymbol{\alpha}_k = \sum_{n=1}^{N} \alpha_{k,n} = 1.0 \quad \forall k \in [1, K], \tag{4}$$

as well as all the end-members

$$\mathbf{1}_L^\top \mathbf{p}_n = 1.0 \quad \forall n \in [1, N], \tag{5}$$

such that from (3)-(5), we have $\mathbf{1}_L^\top \mathbf{y}_k = 1.0$ for all $k \in [1, K]$. The scaled measurements, abundances and noise/uncertainty components in all spatial locations are gathered in the following matrices

$$\mathbf{Y} = \begin{bmatrix} \mathbf{y}_1 & \ldots & \mathbf{y}_K \end{bmatrix} \in \mathbb{R}^{L\times K}, \tag{6}$$

$$\mathbf{A} = \begin{bmatrix} \boldsymbol{\alpha}_1 & \ldots & \boldsymbol{\alpha}_K \end{bmatrix} \in \mathbb{R}^{N\times K}, \tag{7}$$

$$\mathbf{V} = \begin{bmatrix} \mathbf{v}_1 & \ldots & \mathbf{v}_K \end{bmatrix} \in \mathbb{R}^{L\times K}, \tag{8}$$

and as a result, from the linear model in (3), we use a multiplicative structure to model the scaled measurements matrix $\mathbf{Y} = \mathbf{PA} + \mathbf{V}$. In BEAE [3], departing from the information in $\mathbf{Y}$, the matrices ($\mathbf{P}, \mathbf{A}$) are computed based on CQO and ALS by considering a extended maximum likelihood estimation [23].

From (2) and (3), the original measurements $\mathbf{z}_k$ $\forall k \in [1, K]$ are represented by a scaled linear mixture model

$$\mathbf{z}_k = \sum_{n=1}^{N} \underbrace{s_k \alpha_{k,n}}_{\bar{\alpha}_{k,n}} \mathbf{p}_n + \underbrace{s_k \mathbf{v}_k}_{\boldsymbol{\omega}_k} = \sum_{n=1}^{N} \bar{\alpha}_{k,n} \mathbf{p}_n + \boldsymbol{\omega}_k \tag{9}$$

where the scaled abundances $\bar{\alpha}_{k,n}$ are just positive values that indicate the contribution of the n-th end-member $\mathbf{p}_n$ in the k-th spatial location, and the scaled noise/uncertainty vector $\boldsymbol{\omega}_k$ preserves its i.i.d. property. In a matrix/vector notation, the original measurements matrix $\mathbf{Z} = [\mathbf{z}_1 \ \ldots \ \mathbf{z}_K] \in \mathbb{R}^{L\times K}$ is then expressed as

$$\mathbf{Z} = \mathbf{PAS} + \boldsymbol{\Omega} \tag{10}$$

where $\mathbf{S} = \text{diag}([s_1 \ \ldots \ s_K]) \in \mathbb{R}^{K\times K}$ is the scaling matrix (*known directly from the dataset*), and $\boldsymbol{\Omega} = [\boldsymbol{\omega}_1 \ \ldots \ \boldsymbol{\omega}_K] \in \mathbb{R}^{L\times K}$ the uncertainty/noise component.

Now, in this contribution, we present the EBEAE strategy by modifying the cost function in [3], in which a new term is included to rmaximize the entropy of the abundances in each spatial location [2], [24], and the approximation error is normalized. With these changes, the selection of the hyper-parameters will be less sensitive to the experimental dataset, and the classification capabilities will be improved. The EBEAE synthesis problem is described next

$$\min_{\mathbf{P},\mathbf{A}} J(\mathbf{A}, \mathbf{P}) \tag{11}$$

where

$$J(\mathbf{A}, \mathbf{P}) \triangleq \frac{1}{2K} \sum_{k=1}^{K} \frac{\|\mathbf{y}_k - \mathbf{P}\boldsymbol{\alpha}_k\|^2}{\|\mathbf{y}_k\|^2} - \frac{\mu}{2K} \sum_{k=1}^{K} \|\boldsymbol{\alpha}_k\|^2 + \frac{\rho}{2\vartheta} \sum_{n=1}^{N-1} \sum_{j=n+1}^{N} \|\mathbf{p}_n - \mathbf{p}_j\|^2, \tag{12}$$

and

$$\vartheta \triangleq \begin{cases} (N-1) + \cdots + 1 & N \geq 3 \\ 1 & N = 2, \end{cases} \tag{13}$$

constrained to

$$\mathbf{A}^\top \mathbf{1}_N = \mathbf{1}_K, \quad \mathbf{A} \geq 0 \tag{14}$$

$$\mathbf{P}^\top \mathbf{1}_L = \mathbf{1}_N, \quad \mathbf{P} \geq 0. \tag{15}$$

By recalling [3], the cost function in (12) can also be written as

$$J(\mathbf{A}, \mathbf{P}) = \frac{1}{2}\text{Tr}\left\{(\mathbf{Y} - \mathbf{PA})\mathbf{W}(\mathbf{Y} - \mathbf{PA})^\top\right\} - \frac{\mu}{2K}\text{Tr}\left\{\mathbf{AA}^\top\right\} + \frac{\rho}{2\vartheta}\text{Tr}\left\{\mathbf{POP}^\top\right\} \tag{16}$$

where $\mathbf{W} \triangleq (1/K)\text{diag}([1/\|\mathbf{y}_1\|^2 \ \ldots \ 1/\|\mathbf{y}_K\|^2])$ and $\mathbf{O} \triangleq N\mathbf{I}_N - \mathbf{1}_N\mathbf{1}_N^\top$. In (12) or (16), there are only three hyper-parameters N, $\mu \geq 0$ and $\rho \geq 0$ that will control the order in the linear mixture model, the priority in the maximization of the abundances entropy, and the similarity in the resulting end-members, respectively.

To solve (12) or (16), an ALS strategy is considered by adopting a combined local vs. global perspectives in each iteration until convergence [22], [25]:

- If the end-member matrix $\mathbf{P}$ is fixed in (12), the abundance vector $\boldsymbol{\alpha}_k$ in k-th spatial location is independent from the rest. Hence all the abundance vectors $\{\boldsymbol{\alpha}_k\}_{k=1}^K$ are estimated locally for each spatial measurement.
- Meanwhile, if the abundance matrix $\mathbf{A}$ is fixed, the end-member matrix $\mathbf{P}$ is estimated by considering all the measurements in $\mathbf{Y}$ with a global technique.

A. ABUNDANCES EXTRACTION

In this section, we assume that the end-member matrix $\mathbf{P}$ is known and fixed, and the cost-function in (12) is written just with respect to the abundances in the k-th spatial location:

$$\min_{\boldsymbol{\alpha}_k \geq 0,\ \boldsymbol{\alpha}_k^\top \mathbf{1}_N = 1} \frac{1}{2} \frac{\|\mathbf{y}_k - \mathbf{P}\boldsymbol{\alpha}_k\|^2}{\|\mathbf{y}_k\|^2} - \frac{\mu}{2}\|\boldsymbol{\alpha}_k\|^2. \tag{17}$$

This optimization problem is a constrained quadratic formulation [26], whose solution can be deduced by including a Lagrange multiplier $\delta > 0$ in (17) related to the equality

restriction. The stationary conditions are then expressed by a set of linear equations

$$\begin{bmatrix} \frac{1}{y_k}\mathbf{P}^\top\mathbf{P} - \mu\mathbf{I}_N & \mathbf{1}_N \\ \mathbf{1}_N^\top & 0 \end{bmatrix} \begin{bmatrix} \boldsymbol{\alpha}_k \\ \delta \end{bmatrix} = \begin{bmatrix} \frac{1}{y_k}\mathbf{P}^\top\mathbf{y}_k \\ 1.0 \end{bmatrix} \tag{18}$$

where $y_k \triangleq \|\mathbf{y}_k\|^2$. The hyper-parameter μ in (17) is redefined as

$$\mu = \frac{\lambda_{min}(\mathbf{P}^\top\mathbf{P})}{y_k}\bar{\mu} \geq 0 \tag{19}$$

where $\bar{\mu} \in [0, 1)$ is a new normalized parameter, and since $\text{rank}(\mathbf{P}) = N$, we have $\lambda_{min}(\mathbf{P}^\top\mathbf{P}) > 0$. In this way, if $\bar{\mu} = 0$, there is no weight on the abundances entropy, and $\bar{\mu} \approx 1$ will induce a maximal entropy condition during the optimization. The solution to (18) is given by

$$\boldsymbol{\alpha}_k = \boldsymbol{\Phi} \cdot \left(\mathbf{P}^\top\mathbf{y}_k - \frac{\mathbf{y}_k^\top\mathbf{P}\boldsymbol{\Phi}\mathbf{1}_N - 1.0}{\mathbf{1}_N^\top\boldsymbol{\Phi}\mathbf{1}_N}\mathbf{1}_N \right) \tag{20}$$

where $\boldsymbol{\Phi} \triangleq \left(\mathbf{P}^\top\mathbf{P} - \bar{\mu}\lambda_{min}(\mathbf{P}^\top\mathbf{P})\mathbf{I}_N\right)^{-1} \in \mathbb{R}^{N\times N}$. If any entry in the optimal abundance vector in (20) is negative, the linear equations system in (18) is augmented to restrict this element to zero, and the solution is recomputed, as was suggested in [27].

B. END-MEMBERS ESTIMATION

Now, we assume that the abundances matrix $\mathbf{A}$ is known and fixed, and the cost-function in (16) is written with respect to the end-members matrix $\mathbf{P}$:

$$\min_{\mathbf{P}\geq 0,\ \mathbf{P}^\top\mathbf{1}_L = \mathbf{1}_N} \frac{1}{2}\text{Tr}\left\{(\mathbf{Y} - \mathbf{PA})\mathbf{W}(\mathbf{Y} - \mathbf{PA})^\top\right\} + \frac{\rho}{2\vartheta}\text{Tr}\left\{\mathbf{POP}^\top\right\}. \tag{21}$$

Once more, a Lagrange multiplier is added to consider the equality restriction [26], but in this case, the new variable is a vector $\boldsymbol{\chi} \in \mathbb{R}^L$. Due to the quadratic structure in (21), the stationary restrictions are linear in the unknown variables $(\mathbf{P}, \boldsymbol{\chi})$:

$$\mathbf{P}\left(\mathbf{AWA}^\top + \frac{\rho}{\vartheta}\mathbf{O}\right) - \mathbf{YWA}^\top + \mathbf{1}_L\boldsymbol{\chi}^\top = \mathbf{0} \tag{22}$$

$$\mathbf{P}^\top\mathbf{1}_L - \mathbf{1}_N = \mathbf{0}. \tag{23}$$

Hence after solving (22)-(23), we obtain the optimal end-member matrix

$$\mathbf{P} = \left(\mathbf{I}_L - \frac{1}{L}\mathbf{1}_L\mathbf{1}_L^\top\right)\mathbf{YWA}^\top\left(\mathbf{AWA}^\top + \frac{\rho}{\vartheta}\mathbf{O}\right)^{-1} + \frac{1}{L}\mathbf{1}_L\mathbf{1}_N^\top. \tag{24}$$

In the structure of (24), a parameter $\rho \approx 1$ will induce estimated end-members with similar temporal, spectral and/or morphological characteristics among them, and $\rho \approx 0$ the opposite pattern. Similarly to [3], if a matrix element in (24) is negative, the component is set to zero and the column is next normalized to sum-to-one. By the structure of (24), as long as $\text{rank}(\mathbf{YWA}^\top) = N$ and $L > N$, the resulting matrix $\mathbf{P}$ will satisfy $\text{rank}(\mathbf{P}) = N$.

C. IMPLEMENTATION

For the implementation of EBEAE, there are three important steps:

A) The selection of the initialization matrix $\hat{\mathbf{P}}_0$, where this matrix can be obtained from the original measurements $\{\mathbf{z}_k\}_{k=1}^K$ or from previous knowledge of the dataset. For this step, five strategies are suggested: **(I)** The mean measurement in $\mathcal{Z}$ is used as starting component, and then there are selected the remaining $N-1$ terms with the minimum cosine similarity metric (CSM) from this mean component and subsequent elements in $\mathcal{Z}$, until $\hat{\mathbf{P}}_0$ is fully constructed; **(II)** the measurements with the maximum and minimum accumulated intensities are chosen first, and then the remaining ones are chosen with the minimum CSM in $\mathcal{Z}$; **(III)** the left-singular vectors (LSV) of the scaled measurements matrix $\mathbf{Y}$ are used in the initial matrix $\hat{\mathbf{P}}_0$; **(IV)** the sources matrix in the ICA methodology for the scaled measurements matrix $\mathbf{Y}$ is employed as the initial matrix $\hat{\mathbf{P}}_0$ [14], [15]; and **(V)** the user provides the initial matrix $\hat{\mathbf{P}}_0$. Next, each column in $\hat{\mathbf{P}}_0$ is processed by a rectifier function to guarantee non-negative vectors, and normalized to sum-to-one to obtain the initial end-members matrix $\mathbf{P}_0$ for the ALS formulation.

B) The computation of the end-member matrix $\mathbf{P}$, where this matrix is estimated first inside the ALS approach by using a random subset $\hat{\mathcal{Y}} \subset \mathcal{Y}$ with $\hat{K}$ numbers of samples (i.e. $\hat{K} = \text{card}(\hat{\mathcal{Y}})$ where $\hat{K} < K$). The corresponding measurements and abundance matrices over $\hat{\mathcal{Y}}$ are denoted as $\hat{\mathbf{Y}}$ and $\hat{\mathbf{A}}$. If $(\mathbf{P}^i, \hat{\mathbf{A}}^i)$ are the estimates at the i-th iteration of the ALS scheme by solving (17) and (21), the convergence is evaluated with respect to the estimation error at the actual $J_i = \|\mathbf{Y} - \mathbf{P}^i\hat{\mathbf{A}}^i\|_F$ and previous $J_{i-1} = \|\mathbf{Y} - \mathbf{P}^{i-1}\hat{\mathbf{A}}^{i-1}\|_F$ iterations, such that

$$\frac{J_{i-1} - J_i}{J_{i-1}} < \epsilon \tag{25}$$

where $\epsilon > 0$ is the convergence threshold, or if a maximum number of iterations is reached.

C) The estimation of the complete abundance matrix $\mathbf{A}$, where this final step is obtained, once $\mathbf{P}$ is defined by considering all the dataset $\mathcal{Y}$ in (17), and computing the corresponding abundances $\{\boldsymbol{\alpha}_k\}_{k=1}^K$. Finally, these abundances in $\mathbf{A}$ are scaled by $\mathbf{S}$ to reproduce the original dataset $\mathcal{Z}$ according to (10).

A block diagram of the EBEAE implementation is illustrated in Fig. 1. In fact, the initialization step in A) is critical, as was pointed out in previous studies for end-members extraction methods [28], [29]. The four schemes to construct $\hat{\mathbf{P}}_0$ in step A) have interesting interpretations according to the mixing pattern of the end-members in the sets $\mathcal{Z}$ or $\mathcal{Y}$. In general, we are assuming that the dataset $\mathcal{Z}$ might not contain measurements of pure end-members. So, the approach

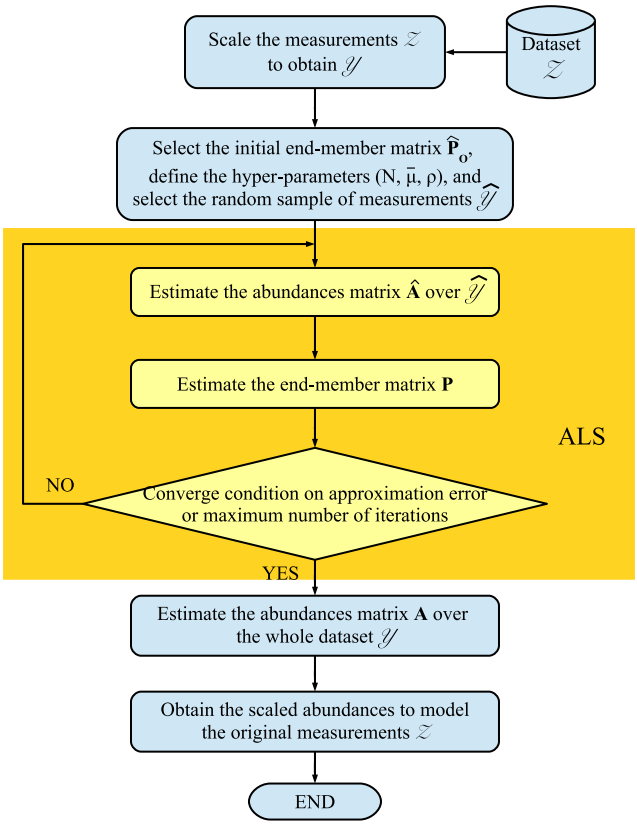

FIGURE 1. Block diagram of the EBEAE implementation.

in **(I)** that departs from the mean measurement in $\mathcal{Z}$ assumes one dominant end-member in the dataset, i.e. its abundance is high in all the measurements. Next, the approach in **(II)** assumes that the measurement intensity is the dominant element to separate the initial end-members, and as a result, the dataset $\mathcal{Z}$ exhibits strong accumulated intensity variations, so the extremes components (measurements with maximum and minimum accumulated intensity) are the best options to initialize the ALS scheme. Meanwhile, the scheme in **(III)** considers the orthonormal vectors with maximal variability for the output space generated by the scaled measurements matrix $\mathbf{Y}$, i.e. related to the temporal-dynamic responses, spectroscopic and/or morphological information. If one orthonomal vector has a negative cumulative sum, all its components are scaled by minus one to obtain a positive orientation. Finally, the proposal in **(IV)** employs the identified sources in the mixing pattern of the ICA formulation as starting matrix [29], where a simple formulation of this algorithm is chosen to reduce the complexity in EBEAE [15]. Nonetheless, other initialization procedures could be pursued by pre-processing the dataset $\mathcal{Z}$, for example the ones reviewed in [28].

III. RESULTS

In this section, we demonstrate initially the application of EBEAE to synthetic datasets. For this purpose, we reproduce synthetically two optical imaging modalities: m-FLIM and HSI samples. In a second stage, we evaluate with three experimental datasets: m-FLIM, OCT, and HSI. In all the examples, the convergence threshold is set to $\epsilon = 1 \times 10^{-3}$, and the maximum number of iterations in the ALS structure is 50. All the data processing and BLU implementations were carried out in MATLAB.

A. SYNTHETIC EVALUATION

We first evaluate EBEAE under synthetic datasets at different noise types and levels. Moreover, we analyze the effect of the four initialization schemes for the end-members matrix (**I**, **II**, **III**, **IV**) and the hyper-parameters $(\rho, \bar{\mu})$ in the estimated end-members and abundances. In addition, we compare the estimation errors against two state-of-the-art BLU methods: S-NNMF optimized by NNLS [18], and a fast version of NS-NNMF based on alternated optimization [19]. To have a fair comparison to EBEAE, the synthetic measurements are scaled prior to the processing of S-NNMF and NS-NNMF. Furthermore, the resulting matrix decompositions by S-NNMF and NS-NNMF do not have inherently the normalization of end-members and abundances of EBEAE. Hence, if $\mathbf{Y} = \mathbf{U} \cdot \mathbf{H}$ denotes the decompositions by S-NNMF and NS-NNMF, the columns of $\mathbf{U}$ and $\mathbf{H}$ are scaled to sum-to-one prior to compute the end-member and abundances estimation errors.

To start the synthetic evaluation, we reproduce m-FLIM datasets where the fluorescence decays are assumed at three spectral bands with four end-members ($N = 4$) [30], [31]. Each synthetic dataset has a spatial dimension 100×100, and 186 time samples by spectral band, i.e. $K = 100 \cdot 100$. The fluorescence decays per spectral bands are concatenated in each synthetic measurement, i.e. $L = 3 \cdot 186$. Two types of additive noise are applied to each dataset: Gaussian and shot noise [31], [32]. In this way, if $\mathbf{z}_k^o$ denotes the ground-truth measurement, then the noisy one $\mathbf{z}_k$ is built as

$$\mathbf{z}_k = \mathbf{z}_k^o + \mathbf{n}_k + \mathbf{m}_k \cdot \sqrt{\mathbf{z}_k^o} \quad k \in [1, K] \tag{26}$$

where $\mathbf{n}_k \in \mathbb{R}^L$ and $\mathbf{m}_k \in \mathbb{R}^L$ represent vectors associated to the noise components, respectively, and the product in $\mathbf{m}_k \cdot \sqrt{\mathbf{z}_k^o}$ is computed component-wise. The Gaussian noise vector $\mathbf{n}_k$ is assumed zero-mean and its standard deviation is assigned according to a given signal-to-noise ratio (SNR):

$$\sigma_k^{SNR} = \sqrt{\frac{\|\mathbf{z}_k^o\|^2}{10^{SNR/10}}}, \tag{27}$$

i.e. $\mathbf{n}_k \sim \mathcal{N}(\mathbf{0}, (\sigma_k^{SNR})^2 \cdot \mathbf{I})$. Meanwhile, the component $\mathbf{m}_k$ related to shot noise is also defined by a zero-mean Gaussian vector with standard deviation defined by an specific peak signal-to-noise ratio (PSNR):

$$\sigma_k^{PSNR} = \sqrt{\frac{\max_{l \in [1,L]}(\mathbf{z}_k^o)_l}{10^{PSNR/10}}}, \tag{28}$$

i.e. $\mathbf{m}_k \sim \mathcal{N}\left(\mathbf{0}, (\sigma_k^{PSNR})^2 \cdot \mathbf{I}\right)$.

After adding the noise components, and for each synthetic dataset, the EBEAE is applied to the scaled measurements matrix $\mathbf{Y}$, where in our evaluation, we have ground-truth sets of end-members $\bar{\mathcal{P}} = \{\bar{\mathbf{p}}_1, \ldots, \bar{\mathbf{p}}_n\}$, i.e. $\bar{\mathbf{p}}_j \in \mathbb{R}^L$ available.

Also, we extract the row vectors of abundance in the dataset for each end-member to generate $\bar{\mathcal{A}} = \{\bar{\boldsymbol{a}}_1, \ldots, \bar{\boldsymbol{a}}_n\}$, i.e. $\bar{\boldsymbol{a}}_j \in \mathbb{R}^{1\times K}$ $\forall j \in [1, n]$. Hence, if the estimated sets of end-members and abundances by EBEAE are $\mathcal{P} = \{\mathbf{p}_1, \ldots, \mathbf{p}_n\}$ and $\mathcal{A} = \{\boldsymbol{a}_1, \ldots, \boldsymbol{a}_n\}$, then the estimation errors are defined as [33]:

$$E_p = \frac{1}{\text{card}(\bar{\mathcal{P}}) + \text{card}(\mathcal{P})} \min_{\forall \bar{\mathbf{p}}\in\bar{\mathcal{P}},\ \mathbf{p}\in\mathcal{P}} \|\bar{\mathbf{p}} - \mathbf{p}\| \quad (29)$$

$$E_a = \frac{1}{\text{card}(\bar{\mathcal{A}}) + \text{card}(\mathcal{A})} \min_{\forall \bar{\boldsymbol{a}}\in\bar{\mathcal{A}},\ \boldsymbol{a}\in\mathcal{A}} \|\bar{\boldsymbol{a}} - \boldsymbol{a}\|. \quad (30)$$

Note that these previous metrics are relevant since the order of end-members in $\bar{\mathcal{P}}$ and $\mathcal{P}$, and of the corresponding abundances in $\bar{\mathcal{A}}$ and $\mathcal{A}$ might not be the same, so a direct pairwise comparison is not feasible.

As a first step, we investigate the relation among initialization process of end-members matrix, and hyper-parameters $(\rho, \bar{\mu})$, as a function of SNR and PSNR. For this purpose, as suggested in [31], [32], we consider different noise levels: (a) SNR $\in \{45, 50, 55\}$ dB and (b) PSNR $\in \{20, 25, 30\}$ dB, which are challenging conditions for EBEAE, especially for the variability induced by the shot noise at large intensity values. We constructed the ground-truth end-members and their abundance maps for the four components, as shown in Figs. 2 and 3 (top panels in the figures), such that each end-member has a spatial area of maximum abundance in the synthetic dataset. The synthetic end-members are overlapping in the three response bands (see top panel in Fig. 3), so this scenario is quite difficult for any BLU algorithm in the state-of-the-art. For each combination of SNR and PSNR, a Monte Carlo evaluation was carried out for the estimation errors E_p and E_a over 25 noise realizations, and the mean and standard deviation of these errors are reported.

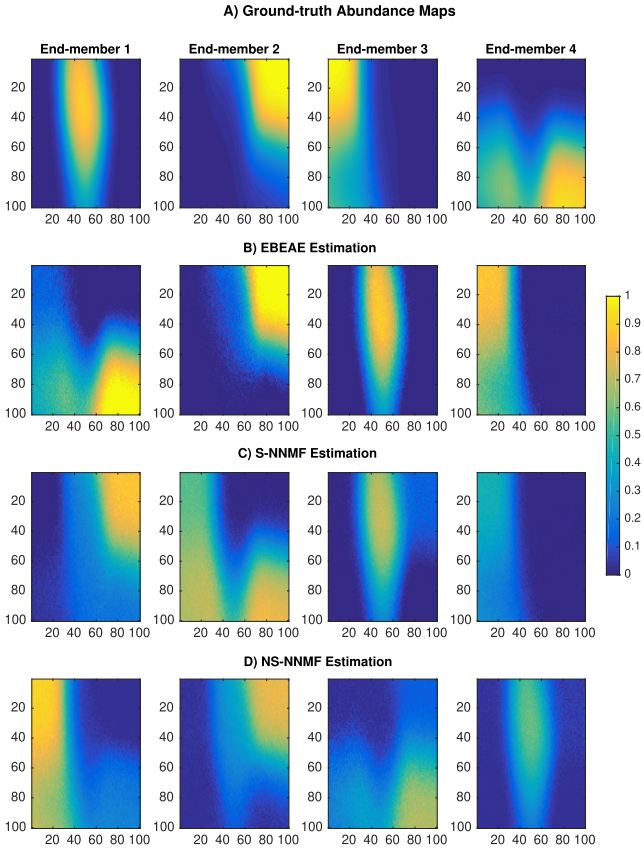

FIGURE 2. One realization of the monte carlo estimation results (abundance maps) for m-FLIM synthetic datasets (N=4, SNR=50 dB and PSNR=25 dB) with State-of-the-Art BLU algorithms: A) Ground-truth, B) EBAE, C) S-NNFM, and D) NS-NNFM.

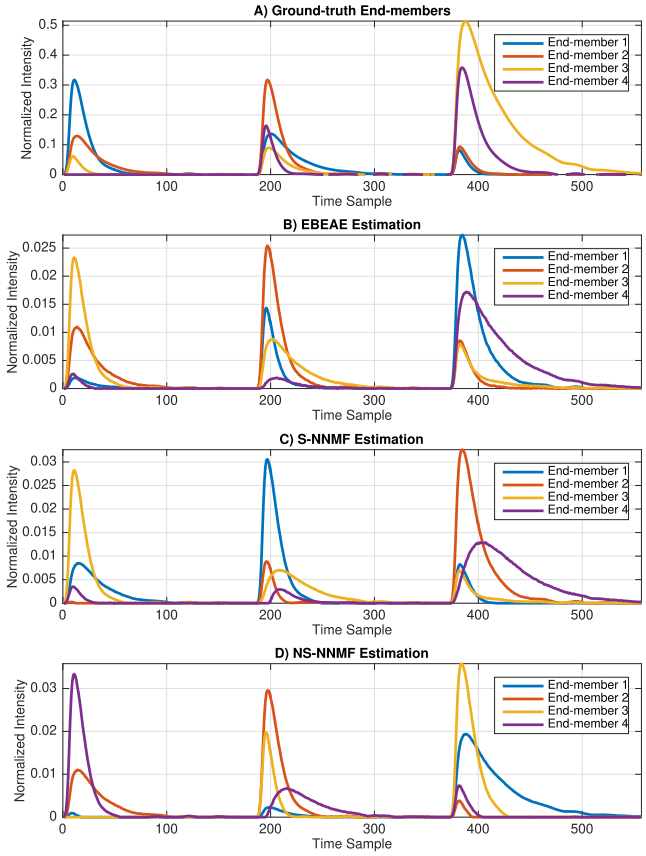

FIGURE 3. One realization of the monte carlo estimation results (end-members) for m-FLIM synthetic datasets (N=4, SNR=50 dB and PSNR=25 dB) with State-of-the-Art BLU algorithms: A) Ground-truth, B) EBAE, C) S-NNFM, and D) NS-NNFM.

In the first evaluation, the EBEAE hyper-parameters were fixed at $\rho = 1.0$ and $\bar{\mu} = 0.0$, and the estimation errors E_p and E_a were computed as a function of the four initialization schemes (**I**, **II**, **III**, **IV**) for the end-members matrix $\hat{\mathbf{P}}_o$. For all four initialization schemes, the mean E_p was consistent to 0.15 in all scenarios despite the noise levels, and just the lowest variability was obtained by initialization **III**. Table 1 illustrates the estimation performance for E_a, where E_p was omitted in the table for brevity. In fact, as the SNR and PSNR increased, the mean value of E_a was constantly reduced for the initializations **I**, **III** and **IV**; although, the mean E_a was more sensitive to PSNR variations. However, the initialization **II**, which depends on the intensity variations per measurement to select the end-members, highlighted the most abrupt error variations in E_a for the SNR and PSNR pairs due to the induced noise. From this evaluation, we observed that

TABLE 1. Monte carlo evaluation of EBEAE estimation error E_a with m-FLIM synthetic datasets ($N = 4$) under Different SNR and PNSR values: Evaluation for initialization conditions I, II, III, and IV ($\rho = 1.0$ and $\bar{\mu} = 0.0$) (*The estimation error with lowest value for each SNR and PSNR combination is highlighted.*).

Noise Level		End-members Initialization			
SNR	PSNR	**I**	**II**	**III**	**IV**
		E_a (mean value $\pm$ standard deviation)			
45	20	0.71 ± 0.15	$\mathbf{0.59 \pm 0.18}$	0.72 ± 0.01	0.77 ± 0.23
45	25	$\mathbf{0.62 \pm 0.07}$	0.83 ± 0.69	0.70 ± 0.01	0.69 ± 0.29
45	30	$\mathbf{0.56 \pm 0.05}$	0.64 ± 0.49	0.66 ± 0.04	0.60 ± 0.32
50	20	$\mathbf{0.64 \pm 0.09}$	0.98 ± 0.63	0.71 ± 0.01	0.72 ± 0.15
50	25	$\mathbf{0.50 \pm 0.02}$	0.51 ± 0.03	0.55 ± 0.01	0.62 ± 0.21
50	30	0.57 ± 0.22	0.65 ± 0.53	$\mathbf{0.48 \pm 0.01}$	0.62 ± 0.28
55	20	$\mathbf{0.64 \pm 0.08}$	0.68 ± 0.10	0.70 ± 0.03	0.69 ± 0.15
55	25	0.52 ± 0.03	0.58 ± 0.30	$\mathbf{0.49 \pm 0.01}$	0.57 ± 0.08
55	30	0.55 ± 0.02	0.63 ± 0.37	$\mathbf{0.47 \pm 0.01}$	0.53 ± 0.11

the lowest variability in E_p and E_a was mainly achieved by initialization **III**.

For this next evaluation, we set the initialization scheme as **III** and defined $\bar{\mu} = 0.0$ to analyze E_p and E_a as a function of the similarity weight $\rho \in \{0.01, 0.10, 1.0, 10.0\}$ for the same SNR and PSNR combinations. Once more, in this testing condition, the changes in ρ did not affect the mean value of $E_p = 0.15$ and just its variability was modified by the pairs (SNR,PSNR). In fact, the variability is quite consistent for $\rho \in \{0.01, 0.10, 1.0\}$ and its raised for $\rho = 10.0$. The performance for E_a is illustrated in Table 2, and it shows that the lowest mean error is achieved in all cases with $\rho = 1.0$.

TABLE 2. Monte carlo results of EBEAE estimation error E_a with m-FLIM synthetic datasets ($N = 4$) under different SNR and PNSR values: Evaluation for different similarity weights ρ (initialization **III** and $\bar{\mu} = 0.0$) (*The estimation error with lowest value for each SNR and PSNR combination is highlighted.*).

Noise level		Similarity Weight ρ			
SNR	PSNR	$\rho = 0.01$	$\rho = 0.1$	$\rho = 1.0$	$\rho = 10$
		E_a (mean value $\pm$ standard deviation)			
45	20	0.88 ± 0.01	0.86 ± 0.01	$\mathbf{0.72 \pm 0.01}$	1.08 ± 0.01
45	25	0.85 ± 0.01	0.83 ± 0.01	$\mathbf{0.69 \pm 0.03}$	1.07 ± 0.01
45	30	0.84 ± 0.01	0.81 ± 0.01	$\mathbf{0.65 \pm 0.03}$	1.07 ± 0.01
50	20	0.86 ± 0.01	0.84 ± 0.01	$\mathbf{0.70 \pm 0.02}$	1.07 ± 0.01
50	25	0.82 ± 0.00	0.80 ± 0.00	$\mathbf{0.55 \pm 0.01}$	1.07 ± 0.01
50	30	0.80 ± 0.00	0.78 ± 0.00	$\mathbf{0.47 \pm 0.01}$	1.07 ± 0.01
55	20	0.85 ± 0.01	0.83 ± 0.01	$\mathbf{0.70 \pm 0.02}$	1.07 ± 0.01
55	25	0.81 ± 0.00	0.78 ± 0.00	$\mathbf{0.49 \pm 0.01}$	1.07 ± 0.01
55	30	0.79 ± 0.00	0.77 ± 0.00	$\mathbf{0.47 \pm 0.01}$	1.06 ± 0.01

The last evaluation for the hyper-parameters performance was defined for the entropy weight $\bar{\mu} \in \{0.05, 0.10, 0.15, 0.2\}$ with respect to the (SNR,PSNR) pairs, where the initial end-member matrix was fixed at **III** and $\rho = 1.0$. Our results showed that there is no tendency of $\bar{\mu}$ in E_p for the different pairs (SNR,PSNR), i.e. the mean value of $E_p = 0.15$ was once more achieved in this test. Table 3 illustrates the estimation error E_a for this last scenario. Hence, when the noise level is high, i.e. smaller pairs (SNR,PSNR), the values of $\bar{\mu} \in \{0.10, 0.15\}$ generate smaller errors in E_a. As the noise level is lower, i.e. larger pairs (SNR,PSNR), the beneficial effect of $\bar{\mu}$ is reduced.

TABLE 3. Monte carlo results for EBEAE estimation error E_a with m-FLIM synthetic datasets ($N = 4$) under different SNR and PNSR Values: Evaluation for different entropy weights $\bar{\mu}$ (initialization **III** and $\rho = 1.0$) (*The estimation error with lowest value for each SNR and PSNR combination is highlighted.*).

Noise level		Entropy Weight $\bar{\mu}$			
SNR	PSNR	$\bar{\mu} = 0.05$	$\bar{\mu} = 0.10$	$\bar{\mu} = 0.15$	$\bar{\mu} = 0.20$
		E_a (mean value $\pm$ standard deviation)			
45	20	0.65 ± 0.05	0.57 ± 0.04	$\mathbf{0.55 \pm 0.02}$	0.63 ± 0.03
45	25	0.59 ± 0.03	$\mathbf{0.53 \pm 0.02}$	0.55 ± 0.02	0.64 ± 0.02
45	30	0.55 ± 0.03	$\mathbf{0.51 \pm 0.01}$	0.57 ± 0.01	0.64 ± 0.01
50	20	0.62 ± 0.04	0.55 ± 0.03	$\mathbf{0.55 \pm 0.01}$	0.64 ± 0.02
50	25	$\mathbf{0.49 \pm 0.01}$	0.53 ± 0.01	0.59 ± 0.01	0.65 ± 0.01
50	30	$\mathbf{0.50 \pm 0.01}$	0.56 ± 0.01	0.60 ± 0.01	0.66 ± 0.01
55	20	0.61 ± 0.03	$\mathbf{0.53 \pm 0.02}$	0.56 ± 0.02	0.63 ± 0.02
55	25	$\mathbf{0.49 \pm 0.01}$	0.56 ± 0.01	0.60 ± 0.01	0.66 ± 0.01
55	30	$\mathbf{0.53 \pm 0.01}$	0.57 ± 0.01	0.62 ± 0.02	0.67 ± 0.01

Now the estimation errors E_p and E_a for EBEAE with initialization **III**, and hyper-parameters $\rho = 1.0$ and $\bar{\mu} = 0.1$ were compared for different noise levels with the BLU algorithms (*implemented also in MATLAB*): S-NNMF and NS-NNMF [18], [19]. The hyper-parameters for S-NNMF and NS-NNMF were tuned manually to reduce as much as possible the estimations errors; and they were selected as $\beta = 0.1$ in S-NNMF, and $\theta = 0.1$ in NS-NNMF for the m-FLIM synthetic datasets. For the error E_p, its mean value was the same for the three algorithms ($E_p = 0.15$), but its variability was higher in all scenarios for S-NNMF. Table 4 presents the estimation error E_a for EBEAE, S-NNMF, and NS-NNMF for different (SNR,PSNR) pairs. With respect to the E_a performance, the lowest mean estimation errors were always achieved by EBEAE. One realization of the Monte Carlo evaluation for the estimated abundance maps at SNR=50 dB and PSNR=25 dB is shown in Fig. 2. In this figure, as expected, the order of the estimated end-members is not equal to the ground-truth, but the abundance maps have similar spatial properties. Nonetheless, as pointed out in Table 4, the most accurate estimation of the abundance maps is given by EBEAE compared to the ground-truth.

TABLE 4. Monte carlo evaluation for estimation errors with m-FLIM synthetic datasets ($N = 4$) under different SNR and PNSR values: Comparison with state-of-the-Art BLU algorithms (BEAE: Initialization **III**, $\rho = 1.0$ and $\bar{\mu} = 0.1$) (*The estimation error with lowest value for each SNR and PSNR combination is highlighted.*).

Noise level		BLU Algorithm		
SNR	PSNR	EBEAE	S-NNMF	NS-NNMF
		E_a (mean value $\pm$ standard deviation)		
45	20	$\mathbf{0.59 \pm 0.04}$	1.43 ± 0.70	1.64 ± 0.01
45	25	$\mathbf{0.53 \pm 0.02}$	1.61 ± 0.91	1.65 ± 0.01
45	30	$\mathbf{0.50 \pm 0.01}$	1.98 ± 1.21	1.65 ± 0.00
50	20	$\mathbf{0.55 \pm 0.02}$	1.86 ± 1.24	1.65 ± 0.01
50	25	$\mathbf{0.53 \pm 0.01}$	2.65 ± 1.53	1.65 ± 0.00
50	30	$\mathbf{0.56 \pm 0.01}$	2.74 ± 1.61	1.65 ± 0.00
55	20	$\mathbf{0.53 \pm 0.02}$	2.06 ± 1.30	1.65 ± 0.00
55	25	$\mathbf{0.55 \pm 0.01}$	2.92 ± 1.58	1.65 ± 0.00
55	30	$\mathbf{0.58 \pm 0.01}$	2.91 ± 1.46	1.65 ± 0.00

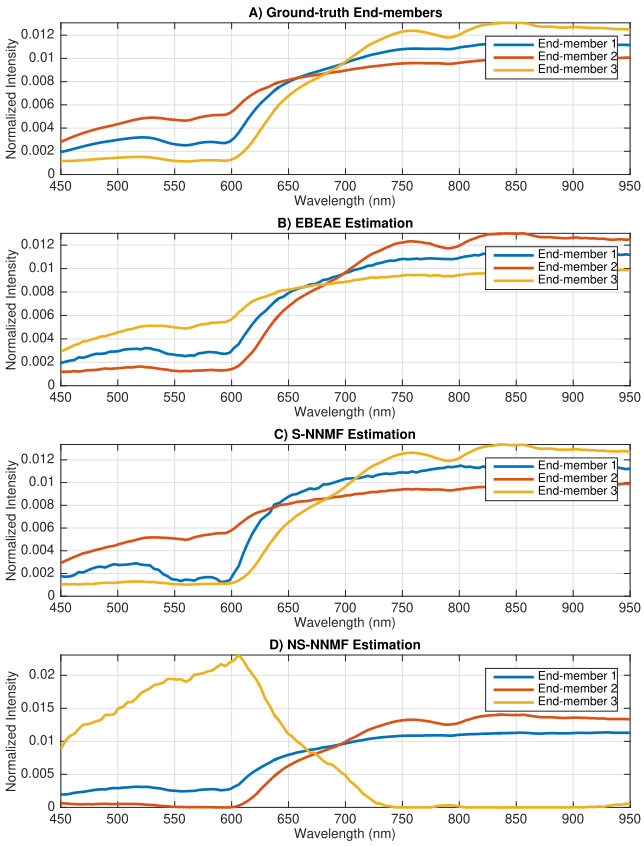

FIGURE 4. One realization of the monte carlo estimation results (end-members) for VNIR synthetic hyperspectral image (N=3, SNR=50 dB and PSNR=25 dB) with State-of-the-Art BLU algorithms: A) Ground-truth, B) EBAE, C) S-NNFM, and D) NS-NNFM.

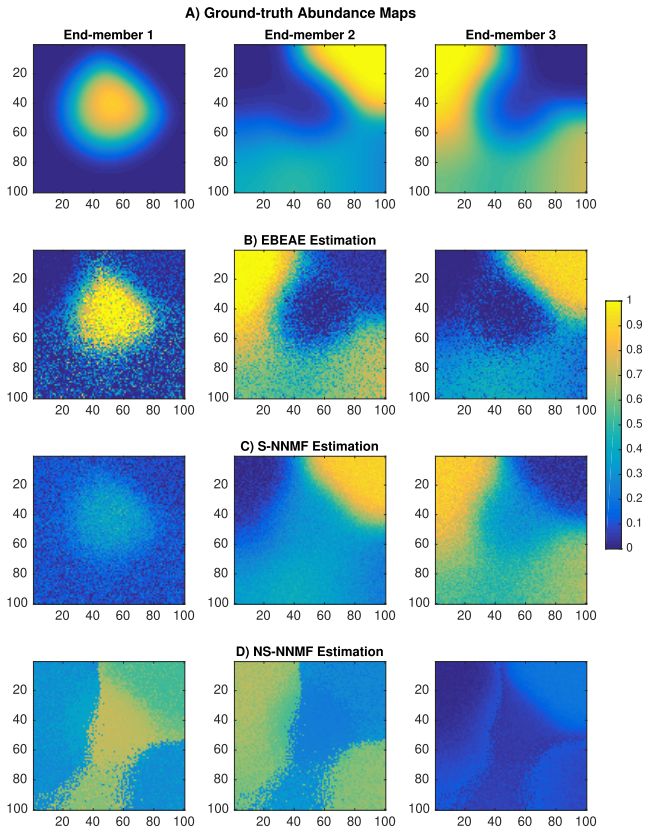

FIGURE 5. One realization of the monte carlo estimation results (abundance maps) for VNIR synthetic hyperspectral image (N=3, SNR=50 dB and PSNR=25 dB) with State-of-the-Art BLU algorithms: A) Ground-truth, B) EBAE, C) S-NNFM, and D) NS-NNFM.

For this same noise level, Fig. 3 presents the estimated end-members for EBEAE, S-NNMF and NS-NNMF, where although the errors E_p are similar for the three BLU algorithms, our proposal has a more accurate characterization specially around the second spectral band.

For this last synthetic evaluation, we generated a visible-near infrared (VNIR) hyperspectral image with three components ($N = 3$). The end-members have spectral responses in the range 450 nm to 950 nm, as shown in the top panel of Fig. 4. These end-members were motivated by the VNIR application for tissue classification in [34], [35]. The evaluation scenario for BLU is quite challenging, since the responses are overlapping in the frequency domain. The ground-truth abundance maps for the three end-members are illustrated in the top panel of Fig. 5. The EBEAE hyper-parameters were slightly tuned to improve the estimation performance: $\rho = 0.1$ and $\bar{\mu} = 0.25$, and the initialization scheme **II** was considered now. Meanwhile, for the other BLU algorithms, the hyper-parameters were tuned also for the best estimation performance: $\beta = 0$ for S-NNMF, and $\theta = 1 \times 10^{-6}$ for NS-NNMF.

A detailed analysis with respect to Gaussian and shot noise was carried out for different combination pairs of (SNR,PSNR). The estimation error results for E_p and E_a of the Monte Carlo analysis with 25 noise realizations for each (SNR,PSNR) pair are presented in Table 5. In this testing scenario, we observed substantial differences in the estimation of the end-members for the BLU algorithms, so we present the E_p performance. The results for E_p clearly show that EBEAE has the lowest mean estimation error, i.e. the most accurate estimation. This conclusion is verified in Fig. 4 for SNR=50 dB and PSNR=25 dB, where the estimated end-members by EBEAE are similar to the ground-truths. Meanwhile, the S-NNMF estimations presented variations in the spectral responses, and NS-NNMF had the poorest performance, since one end-member had a spectral response practically zero in a large wavelength band. As showns Table 5, the abundance error E_a in the majority of the pairs (SNR,PSNR) had the best performance with BEAE, and in just one case S-NNMF obtained the best response, but the difference was quite small. Figure 5 shows the estimated abundance maps for a realization with SNR=50 dB and PSNR=25 dB, where the spatial resolution of the abundance maps by EBEAE was similar to the ground-truths. This same figure illustrates an improved estimation of EBEAE with respect to S-NNMF and NS-NNMF.

In the overall, this exhaustive synthetic evaluation showed how to tune the hyper-parameters of EBEAE, and its

TABLE 5. Monte carlo evaluation of estimation errors E_p and E_a with VNIR synthetic hyperspectral images ($N = 3$) under different SNR and PNSR values: Comparison with State-of-the-Art BLU algorithms (BEAE: Initialization II, $\rho = 0.1$ and $\bar{\mu} = 0.25$) (*The estimation error with lowest value for each SNR and PSNR combination is highlighted.*).

Noise level		BLU Algorithm		
SNR	PSNR	EBEAE	S-NNMF	NS-NNMF
		$E_p \times 10^{-3}$ (mean value $\pm$ standard deviation)		
45	20	**0.17 ± 0.07**	0.40 ± 0.03	0.20 ± 0.08
45	25	**0.15 ± 0.09**	0.42 ± 0.10	0.19 ± 0.08
45	30	**0.14 ± 0.07**	0.44 ± 0.10	0.18 ± 0.04
50	20	**0.13 ± 0.06**	0.31 ± 0.17	0.41 ± 0.07
50	25	**0.11 ± 0.05**	0.34 ± 0.19	0.37 ± 0.10
50	30	**0.15 ± 0.07**	0.33 ± 0.20	0.39 ± 0.09
55	20	**0.10 ± 0.06**	0.24 ± 0.21	0.27 ± 0.12
55	25	**0.09 ± 0.05**	0.34 ± 0.24	0.28 ± 0.12
55	30	**0.12 ± 0.06**	0.32 ± 0.23	0.26 ± 0.11
		E_a (mean value $\pm$ standard deviation)		
45	20	**1.57 ± 0.37**	1.75 ± 0.26	3.06 ± 0.01
45	25	**1.59 ± 0.32**	1.82 ± 0.32	3.06 ± 0.01
45	30	**1.67 ± 0.43**	1.87 ± 0.39	3.06 ± 0.01
50	20	**1.24 ± 0.46**	1.62 ± 0.80	3.06 ± 0.01
50	25	**1.31 ± 0.50**	1.75 ± 0.81	3.05 ± 0.02
50	30	**1.24 ± 0.50**	1.59 ± 0.77	3.06 ± 0.01
55	20	1.82 ± 1.10	**1.33 ± 1.00**	2.99 ± 0.02
55	25	**1.17 ± 0.89**	1.74 ± 1.02	2.99 ± 0.01
55	30	**1.33 ± 0.89**	1.66 ± 1.02	2.99 ± 0.02

advantage in the estimation of end-members and their abundances compared to S-NNMF and NS-NNMF. This improvement is more eloquent in the case of the VNIR datasets, where the end-members had overlapping in their structure. Next, we test with three experimental datasets: m-FLIM, OCT, and HSI, and we focus just on the application of EBEAE.

B. M-FLIM APPLICATION

This experimental biomedical application is focused on imaging the oral cavity to chemically analyse a suspicious lesion. First, a clinician performed a medical examination of the patient. Next, *in-vivo* imaging of clinically suspicious oral lesions was performed using a handheld multispectral FLIM (m-FLIM) endoscope [30]. The imaging system consisted of a handheld box (volume: $7 \times 13 \times 5$ cm^3, mass: 450 g) fitted with a custom-designed rigid endoscope (length: 14 cm; diameter: 1.7 cm). A frequency-tripled Q-switched Nd:YAG laser (355 nm, 1 ns pulse width, 10 kHz max. rep. rate, Advanced Optical Technology) was used as the excitation source. A set of dichroic mirrors and filters separated the emission into three spectral bands (390 ± 20 nm, 452 ± 22.5 nm, and 550 ± 20 nm), each one coupled into separate multimode fibers of different lengths that provide an optical delay between each spectral band. The multispectral fluorescence signal is detected by a multichannel plate photomultiplier tube (25 ps transient time spread, R3809U-50, Hamamatsu), followed by a preamplifier before being digitized at 6.25 GS/s by a high-speed digitizer (PXIe-5185, National Instruments) resulting in a temporal resolution of 160 ps. Two images were acquired per patient, one from the lesion site (*lesion sample*), and one from a normal contralateral site (*contrast sample*)

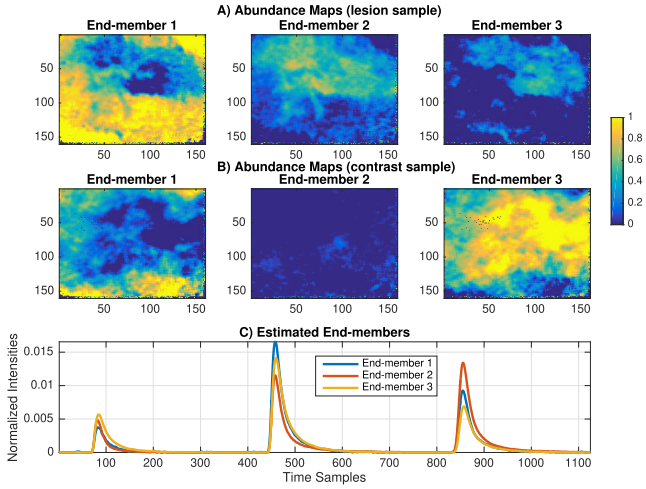

FIGURE 6. EBEAE results for m-FLIM application with initialization (II): Abundance maps in the interval [0, 1] for the three end-members A) lesion sample, B) contrast sample, and C) Estimated end-members (*The abundance maps illustrate the spatial contribution of the corresponding end-member in the sample, where a pixel close to zero corresponds to the absence of the end-member in that point, and a pixel close to one denotes the full concentration of it.*).

in the oral cavity. Finally, a biopsy was taken and sent for histopathological evaluation.

The imaged oral tissue corresponded to a tongue sample which was diagnosed as squamous cell carcinoma (SCC) based on the histopathological evaluation. The m-FLIM database had dimensions $160 \times 160 \times 1,125$, where the first two represent the spatial domain, and the last one the temporal response. The lesion and contrast samples were analyzed simultaneously by EBEAE with the following hyper-parameters: $N = 3$, $\rho = 0.8$ and $\bar{\mu} = 0.2$. These hyper-parameters were slightly tuned departing from the best performance in the synthetic evaluation of the previous section. The results for all the four initialization schemes **I**-**IV** were consistent, and for illustration purposes Figs. 6 and 7 show the BLU with approaches **II** and **III**. Figures 6(A) and (B) highlights the resulting abundance maps for the lesion and contrast samples (top and middle images) and the estimated end-members (bottom plot) for initialization **II**, where the abundance results clearly show different chemometric characterizations for the SCC (lesion) and normal (contrast) tissue samples. Thus, end-member 2 is only present in the SCC (lesion) sample, and end-members 1 and 3 in the contrast one. In fact, the time-profiles of the estimated end-members (see Fig. 6(C)) show that their peak responses are different for each spectral band. Meanwhile, Figs. 7(A) -(C) describe the corresponding BLU for initialization **III**, where just the order of the characteristic end-members and corresponding abundance maps in the SCC (lesion) and normal (contrast) tissue samples is different with respect to Fig. 6. As a result, with this new initialization, end-member 3 is now the distinctive for the SCC (lesion) sample, and once more the end-members illustrate different peak responses in each spectral band. Hence, the EBEAE algorithm detected three distinctive fluorophores

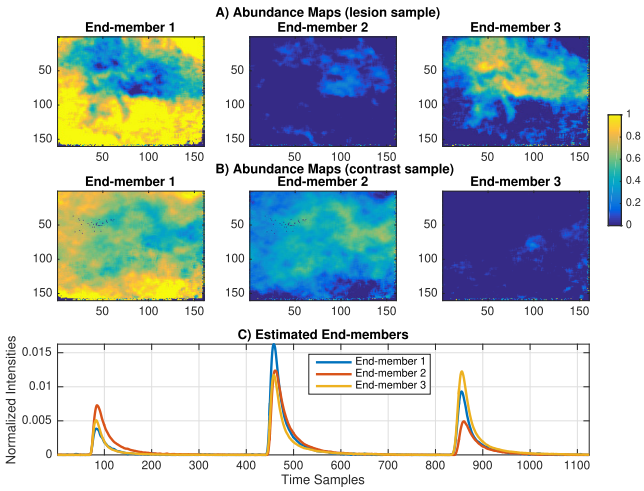

FIGURE 7. EBEAE results for m-FLIM application with initialization (III): Abundance maps in the interval [0, 1] for the three end-members A) lesion sample, B) contrast sample, and C) Estimated end-members.

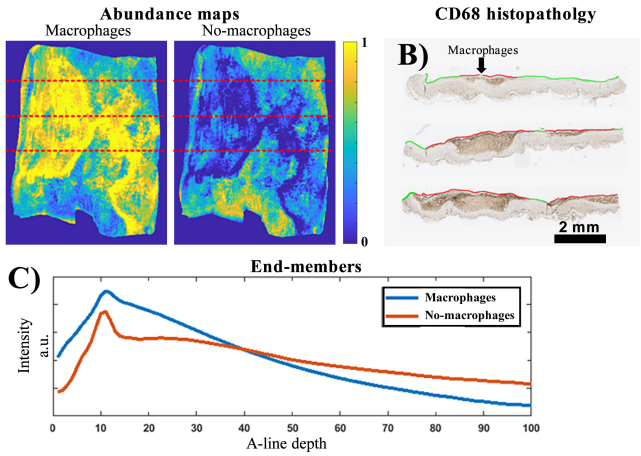

FIGURE 8. EBEAE results for OCT application with initialization (I): A) Abundance maps in the interval [0, 1] for the end-members macrophages and no-macrophages, B) CD68 histological sections corresponding to the dotted lines in A) (*the dark-brown areas highlight high concentration of macrophages*), and C) Estimated end-members.

in both tissue samples by the non-trivial abundance maps and distinctive multi-spectral time-profiles. In fact, the EBEAE algorithm was also implemented with a higher order model $N = 4$, but one of the abundance maps was trivial. As a result, the application of EBEAE successfully provided a quantitative representation of the m-FLIM database and highlighted chemical features for the SCC tissue.

C. OCT APPLICATION

This next biomedical application is aimed to find specific chemical and morphological markers for an early-detection of atherosclerosis [36], [37]. Nonetheless, the focus will be on the morphological structure that an OCT analysis can highlight. The database consisted of images of post-mortem artery samples acquired with a 1,310 nm swept-source OCT imaging system previously described in [37]. The imaged artery segments underwent histopathological processing, and the histological sections were stained with CD68 for labeling macrophages in the sample. The histology sections were cut from specific points previously inked on the right side of the artery lumen, in order to match the histology with the OCT images and abundance maps (dotted lines in Fig. 8(A)). The dimensions of the OCT datasets are 668×800 spatial pixels and 1,024 axial pixels with a resolution of 8.6 μm. The OCT B-scan was initially preprocessed to segment the lumen surface, and align it in all A-lines. Only the first 100 pixels (860 μm) starting from the lumen surface were analyzed by the EBEAE. Since the aim is to the detect the presence of superficial macrophages in the artery sample, a second order mixing model ($N = 2$) is used by the EBEAE algorithm, and the remaining hyper-parameters were $\rho = 0.8$ and $\bar{\mu} = 0.2$ (as in the previous section). In this case, the initialization $\mathbf{I}$, based on the mean measurement in the database, was applied.

Figures 8(A) to (C) show the abundance maps, histopathology evaluation, and estimated end-members by EBEAE, respectively. The presence of macrophages in the artery is characterized by brighter intensity at the beginning of the profile, and a monotonic decaying rate in the A-line depth. Consequently, the end-members in Fig. 8(C) were labeled as macrophages and no-macrophages. The abundance maps and histology sections in Figs. 8(A) and (B) illustrate an agreement to detect the macrophages in the imaged sample. Once more, the EBEAE was able to accurately and quantitatively characterize the sample for this application.

D. HSI APPLICATION

The last application of EBEAE in this work describes the use of HSI to guide a neurosurgeon to define brain tumour margins in a surgical procedure [34], [35]. For this purpose, a VNIR pushbroom camera is used over the spectral range from 400 nm to 1,000 nm (a spectral resolution of 2–3 nm) to capture 826 spectral bands and 1,004 spatial pixels per line. The measured HSI shows an *in-vivo* brain surface of an adult patient undergoing craniotomy for resection of intra-axial brain tumor. After cropping the parenchyma section, the HSI database with size $377 \times 329 \times 826$, being the first two the spatial dimensions and the third one the spectral dimension, was pre-processed before the EBEAE analysis by a five stages procedure [35]: (i) a radiometric calibration, (ii) a noise filtering step, (iii) a reduction of the spectral interval, (iv) a spectral averaging between contiguous bands, and (v) an intensity normalization. Consequently, the final database had 129 spectral bands. Some parts of the image were labeled by using a semi-automatic tool developed to this end [38]. Hence, a golden standard map gathered four classes: normal tissue (NT), tumor tissue (TT), blood vessel (BV), and background (BG). The class BG includes diverse substances or materials not relevant for the tumor resection procedure, as skull bone, dura, skin, or surgical material [34], [35]. Figures 9(A) and (B) show a synthetic RGB representation (*false color*) of the studied image, and the resulting golden standard map. This labeling was performed by a

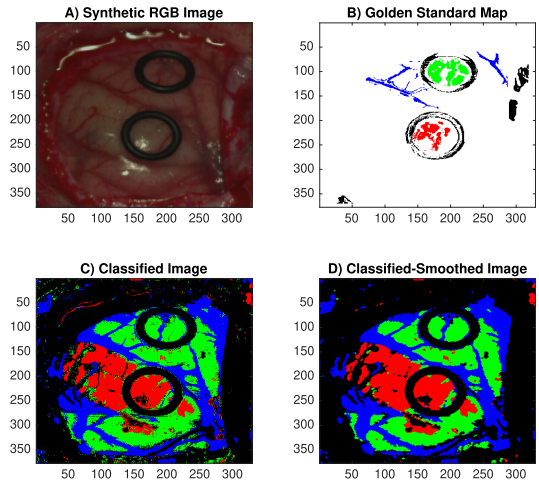

FIGURE 9. **EBEAE results for hyperspectral images: A) Synthetic RGB Image (*false color*), B) Golden Standard Map, C) Classified Image (Green -Normal Tissue, Red- Tumor Tissue, Blue - Blood Vessel, Black - Background), and D) Classified and Smoothed Image (*The rubber ring markers presented in A) were employed by the neurosurgeons to identify the location where the biopsy was performed for the histopathological assessment.*).**

neurosurgeon using the previously mentioned tool, and the final diagnosis was assessed though histopathological analysis of tissue. All the selected pixels for NT, TT and BV classes showed a consistent spectral response, except for the BG class which presented a diverse spectral pattern in the labeled pixels.

Based on these selected pixels for classes NT, TT and BV, an average spectral response was generated to identify representative end-members $\{\mathbf{p}_{NT}, \mathbf{p}_{TT}, \mathbf{p}_{BV}\}$. By its spectral diverse pattern, the EBEAE was applied just to estimate end-members for the BG class, with the following hyper-parameters $N = 4$, $\rho = 0.01$ and $\bar{\mu} = 0$, and initialization **II**. The similarity weight ρ was chosen small to allow diversity in the estimated end-members, and the entropy weight $\bar{\mu}$ was null to search for the minimum estimation error. As a result, EBEAE provided four end-members for the BG class $\{\mathbf{p}^1_{BG}, \mathbf{p}^2_{BG}, \mathbf{p}^3_{BG}, \mathbf{p}^4_{BG}\}$.

Next, the end-members matrix $\mathbf{P}$ was constructed with seven spectral profiles

$$\{\mathbf{p}_{NT}, \mathbf{p}_{TT}, \mathbf{p}_{BV}\} \bigcup \{\mathbf{p}^1_{BG}, \mathbf{p}^2_{BG}, \mathbf{p}^3_{BG}, \mathbf{p}^4_{BG}\},$$

which described the four classes of studied tissue in the HSI database. To identify the abundance of each class, the estimation algorithm in (17) is just computed with $\bar{\mu} = 0.2$. For the BG class, the corresponding abundance per pixel of the four profiles $\{\mathbf{p}^1_{BG}, \mathbf{p}^2_{BG}, \mathbf{p}^3_{BG}, \mathbf{p}^4_{BG}\}$ were added together. Figures 10(A) and (B) show the resulting abundance maps and the seven estimated end-members. Finally, to obtain a hard classification, each pixel was labeled as (NT, TT, BV, BG) according to the maximum abundance per pixel, and to smooth the classified regions, morphological close and open operators with a disk-shaped structuring element of 1 pixel of radius were lastly applied in sequence [39]. Figures 9(C) and (D) illustrate the classified and classified-smoothed images, respectively, which as

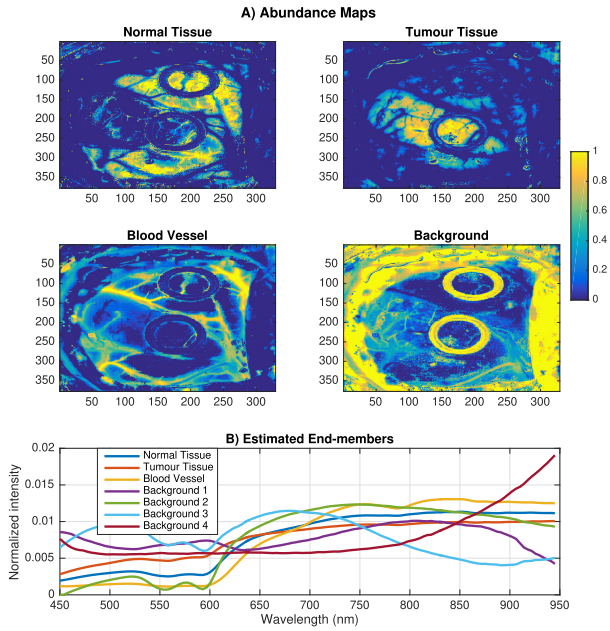

FIGURE 10. **EBEAE results for hyperspectral images: A) Abundance maps in the interval [0, 1] for the four classes (Normal Tissue, Tumor Tissue, Blood Vessel, Background), and B) Estimated end-members per class (*The abundance maps illustrate the spatial contribution of the corresponding end-member in the sample, where a pixel close to zero corresponds to the absence of the end-member in that point, and a pixel close to one denotes the full concentration of it.*).**

expected are consistent with the golden standard map and the previous result in [34]. One important advantage of this EBEAE application is its low complexity to achieve the classified image; since in [34], this labeled map requires a dimentionality reduction, a K-nearest neighbor clustering, and a support-vector machine classification.

IV. CONCLUSION

In this work, the EBEAE methodology was introduced to address the BLU problem in biomedical optical imaging applications subject to positivity constraints. The mathematical formulation of EBEAE was based on CQO and ALS algorithms. In this formulation, a local approach was used to estimate the abundances of each end-member in the measurements by reducing the approximation error and maximizing their entropy, and a global technique to iteratively identify the end-members by minimizing the similarity among them and also the approximation error. The optimization cost functions were normalized to avoid the dependence on the dataset size, and four initialization approaches were suggested for the end-members matrix. There are three hyper-parameters in EBEAE $(N, \rho, \bar{\mu})$. The values of (N, ρ) are selected according to some a piori information of the dataset. Hence, the parameter N defines the order of the linear mixture model, i.e. the number of end-members that are assumed in the dataset. Parameter ρ is a positive value, which is close to zero if the end-members are assumed with different temporal-dynamic responses, spectroscopic and/or morphological characteristics among them, and close to one otherwise. Meanwhile, $\bar{\mu} \in [0, 1)$ is a parameter related

to the entropy of the resulting abundances, so a value close to one induces a maximal entropy during the estimation process, and close to zero discards this property. Finally, the initial end-members matrices were suggested by assuming certain structure in the dataset: (i) there is a dominant end-member in the samples, (ii) the intensity variations in the measurements are related to the end-members presence, (iii) the end-members are orthogonal with maximal variability in the measurements space, and (iv) the end-members are statistically independent (*ICA perspective*). The effect of the hyper-parameters and initialization schemes in EBEAE was analyzed under synthetic datasets at different noise types and levels. In addition, the advantage of EBEAE was highlighted against two state-of-the-art BLU algorithms (S-NNMF and NS-NNMF) for the synthetic datasets. To show the generality of EBEAE, three diverse biomedical imaging applications were demonstrated experimentally: m-FLIM for chemometric analysis in oral cavity samples, OCT for macrophages identification in post-mortem artery samples, and HSI for *in-vivo* brain tissue classification and tumor identification. In all the examples, EBEAE was able to provide a quantitative analysis of the samples with none or minimal a priori information. The future work in this research line will focus on implementing a parallel version of EBEAE for the goal of a real-time application, and applying EBEAE in other biomedical engineering scenarios.

REFERENCES

[1] Y. Zhang, C. Sun, D. Yang, and H. Qu, "Multiband imaging and linear unmixing of optical fiber intrusion signal," *Optik*, vol. 167, pp. 60–72, Aug. 2018.

[2] J. J. Rico-Jimenez, D. U. Campos-Delgado, M. Villiger, K. Otsuka, B. E. Bouma, and J. A. Jo, "Automatic classification of atherosclerotic plaques imaged with intravascular OCT," *Biomed. Opt. Express*, vol. 7, no. 10, pp. 4069–4085, 2016.

[3] O. Gutierrez-Navarro, D. U. Campos-Delgado, E. Arce-Santana, M. Mendez, and J. A. Jo, "Blind end-member and abundance extraction for multispectral fluorescence lifetime imaging microscopy data," *IEEE J. Biomed. Health Inform.*, vol. 18, no. 2, pp. 606–617, Mar. 2014.

[4] H. Xu and B. W. Rice, "*In-vivo* fluorescence imaging with a multivariate curve resolution spectral unmixing technique," *J. Biomed. Opt.*, vol. 14, no. 6, 2009, Art. no. 064011.

[5] R. Liang, *Biomedical Optical Imaging Technologies: Design and Applications*. New York, NY, USA: Springer-Verlag, 2013.

[6] A. P. Dhawan, B. D'Alessandro, and X. Fu, "Optical imaging modalities for biomedical applications," *IEEE Rev. Biomed. Eng.*, vol. 3, pp. 69–92, 2010.

[7] C. Balas, "Review of biomedical optical imaging—A powerful, non-invasive, non-ionizing technology for improving *in vivo* diagnosis," *Meas. Sci. Technol.*, vol. 20, no. 10, 2009, Art. no. 104020.

[8] A. Periasamy and R. M. Clegg, *FLIM Microscopy in Biology and Medicine*. London, U.K.: Chapman & Hall, 2009.

[9] J. R. Lakowicz, *Principles of Fluorescence Spectroscopy*. New York, NY, USA: Springer-Verlag, 2006.

[10] O. Gutierrez-Navarro, D. U. Campos-Delgado, E. R. Arce-Satana, and J. A. Jo, "Quadratic linear unmixing: A graphical user interface for tissue characterization," *Comput. Methods Programs Biomed.*, vol. 124, pp. 148–160, Feb. 2016.

[11] T. Pengo, A. M. N. Barrutia, I. Zudaire, and C. O. de Solorzano, "Efficient blind spectral unmixing of fluorescently labeled samples using multi-layer non-negative matrix factorization," *PLoS ONE*, vol. 8, no. 11, 2013, Art. no. e78504.

[12] Z. Yang, G. Zhou, S. Xie, S. Ding, J.-M. Yang, and J. Zhang, "Blind spectral unmixing based on sparse nonnegative matrix factorization," *IEEE Trans. Image Process.*, vol. 20, no. 4, pp. 1112–1125, Apr. 2011.

[13] G. James, D. Witten, T. Hastie, and R. Tibshirani, *An Introduction to Statistical Learning*. New York, NY, USA: Springer-Verlag, 2013.

[14] A. Tharwat, "Independent component analysis: An introduction," *Appl. Comput. Informat.*, to be published.

[15] J. Shlens, "A tutorial on independent component analysis," 2014, *arXiv:1404.2986*. [Online]. Available: https://arxiv.org/abs/1404.2986

[16] N. Gillis, "The why and how of nonnegative matrix factorization," in *Regularization, Optimization, Kernels, and Support Vector Machines* (Machine Learning and Pattern Recognition Series), J. A. K. Suykens, M. Signoretto, and A. Argyriou, Eds. London, U.K.: Chapman & Hall, 2014, pp. 257–291.

[17] Y.-X. Wang and Y.-J. Zhang, "Nonnegative matrix factorization: A comprehensive review," *IEEE Trans. Knowl. Data Eng.*, vol. 25, no. 6, pp. 1336–1353, Jun. 2013.

[18] Y. Y. Li and A. Ngom, "The non-negative matrix factorization toolbox for biological data mining," *Source Code Biol. Med.*, vol. 8, no. 1, pp. 1–10, 2013.

[19] Z. Yang, Y. Zhang, W. Yan, Y. Xiang, and S. Xie, "A fast non-smooth nonnegative matrix factorization for learning sparse representation," *IEEE Access*, vol. 4, pp. 5161–5168, 2016.

[20] M. Berman, H. Kiiveri, R. Lagerstrom, A. Ernst, R. Dunne, and J. F. Huntington, "ICE: A statistical approach to identifying endmembers in hyperspectral images," *IEEE Trans. Geosci. Remote Sens.*, vol. 42, no. 10, pp. 2085–2095, Oct. 2004.

[21] R. Tauler and A. de Juan, "Chapter 5—Multivariate curve resolution for quantitative analysis," in *Data Handling in Science and Technology*, vol. 29, A. M. de la Peña, H. C. Goicoechea, G. M. Escandar, and A. C. Olivieri, Eds. Amsterdam, The Netherlands: Elsevier, 2015, pp. 247–292.

[22] J. Jaumot, R. Gargallo, A. de Juan, and R. Tauler, "A graphical user-friendly interface for MCR-ALS: A new tool for multivariate curve resolution in MATLAB," *Chemometrics Intell. Lab. Syst.*, vol. 76, no. 1, pp. 101–110, 2005.

[23] B. C. Levy, *Principles Signal Detection Parameter Estimation*. New York, NY, USA: Springer-Verlag, 2008.

[24] M. Rivera and O. Dalmau, "Variational viewpoint of the quadratic Markov measure field models: Theory and algorithm," *IEEE Trans. Image Process.*, vol. 2, no. 3, pp. 1246–1257, Mar. 2012.

[25] F. W. Young, J. de Leeuw, and Y. Takane, "Regression with qualitative and quantitative variables: An alternating least squares method with optimal features," *Psychometrika*, vol. 41, no. 4, pp. 505–526, 1976.

[26] J. Nocedal and S. J. Wright, *Numerical Optimization*, 2nd ed. New York, NY, USA: Springer-Verlag, 2006.

[27] O. Gutierrez-Navarro, D. U. C. Delgado, E. Arce-Santana, M. Mendez, and J. A. Jo, "A fully constrained optimization method for time-resolved multispectral fluorescence lifetime imaging microscopy data unmixing," *IEEE Trans. Biomed. Eng.*, vol. 60, no. 6, pp. 1711–1720, Jun. 2013.

[28] A. Plaza and C. I. Chang, "Impact of initialization on design of endmember extraction algorithms," *IEEE Trans. Geosci. Remote Sens.*, vol. 44, no. 11, pp. 3397–3407, Nov. 2006.

[29] L. Valderrama, R. P. Goncalves, P. H. Marco, D. N. Rutledge, and P. Valderrama, "Independent components analysis as a means to have initial estimates for multivariate curve resolution-alternating least squares," *J. Adv. Res.*, vol. 7, no. 5, pp. 795–802, 2016.

[30] J. M. Jabbour, S. Cheng, B. H. Malik, R. Cuenca, J. A. Jo, J. Wright, Y. S. L. Cheng, and K. C. Maitland, "Fluorescence lifetime imaging and reflectance confocal microscopy for multiscale imaging of oral precancer," *J. Biomed. Opt.*, vol. 18, no. 4, 2013, Art. no. 046012.

[31] O. Gutierrez-Navarro, D. U. Campos-Delgado, E. R. Arce-Santana, K. C. Maitland, S. Cheng, J. Jabbour, B. Malik, R. Cuenca, and J. A. Jo, "Estimation of the number of fluorescent end-members for quantitative analysis of multispectral flim data," *Opt. Express*, vol. 22, no. 10, pp. 12255–12272, May 2014.

[32] D. U. Campos-Delgado, O. Gutierrez-Navarro, E. R. Arce-Santana, M. C. Skala, A. J. Walsh, and J. A. Jo, "Blind deconvolution estimation of fluorescence measurements through quadratic programming," *J. Biomed. Opt.*, vol. 20, no. 7, pp. 1–16, 2015.

[33] A. Conci and C. Kubrusly, "Distance between sets—A survey," *Adv. Math. Sci. Appl.*, vol. 26, pp. 1–18, 2017.

[34] H. Fabelo *et al.*, "Spatio-spectral classification of hyperspectral images for brain cancer detection during surgical operations," *PLoS ONE*, vol. 13, no. 3, 2018, Art. no. e0193721.

[35] H. Fabelo *et al.*, "An intraoperative visualization system using hyperspectral imaging to aid in brain tumor delineation," *Sensors*, vol. 18, no. 2, p. 430, 2018.

[36] P. Pande, S. Shrestha, J. Park, I. Gimenez-Conti, J. Brandon, B. E. Applegate, and J. A. Jo, "Automated analysis of multimodal fluorescence lifetime imaging and optical coherence tomography data for the diagnosis of oral cancer in the hamster cheek pouch model," *Biomed. Opt. Express*, vol. 7, no. 5, pp. 2000–2015, 2016.

[37] S. Shrestha, M. J. Serafino, J. J. Rico-Jimenez, J. Park, X. Chen, S. Zhaorigetu, B. L. Walton, J. A. Jo, and B. E. Applegate, "Multimodal optical coherence tomography and fluorescence lifetime imaging with interleaved excitation sources for simultaneous endogenous and exogenous fluorescence," *Biomed. Opt. Express*, vol. 7, no. 9, pp. 3184–3197, 2016.

[38] H. Fabelo *et al.*, "*In-vivo* hyperspectral human brain image database for brain cancer detection," *IEEE Access*, vol. 7, pp. 39098–39116, 2019.

[39] R. C. Gonzalez and R. E. Woods, *Digital Image Processing*, 4th ed. London, U.K.: Pearson, 2017.

DANIEL U. CAMPOS-DELGADO (M'98–SM'13) received the B.S. degree in electronics engineering from the Autonomous University of San Luis Potosi (UASLP), Mexico, in 1996, and the M.S.E.E. and Ph.D. degrees in electrical engineering from Louisiana State University (LSU), USA, in 1999 and 2001, respectively. In 2001, he joined the Faculty of Sciences, UASLP, as a Professor. He has published more than 200 referred articles in scientific journals, and international and national congresses. Since July 2016, he has been the Dean of the Faculty of Sciences. His research interests include estimation and detection, optimization algorithms, fault diagnosis, control theory, and digital signal processing. In these areas, he has received the international funding for collaborative work with the University of California, Santa Barbara, Texas A&M University, and the Institute of Molecular Bioimaging and Physiology, Milan. From August 2014 to May 2015, he was a Visiting Scholar with the Biomedical Engineering Department of Texas A&M University. He has been an Advisor or Co-Advisor of 26 bachelor's thesis project, 22 Master's thesis work, and six Ph.D. dissertations. He is currently a member of the Mexican Academy of Sciences (AMC). In 2001, the College of Engineering of LSU granted him the Exemplary Dissertation Award. In 2009 and 2013, he received the Young Researcher Awards from UASLP and AMC.

OMAR GUTIERREZ-NAVARRO received the B.E. degree in electronics engineering from the Universidad Autónoma de San Luis Potosí (UASLP), San Luis Potosi, Mexico, the M.Sc. degree in computer science and industrial mathematics from the Centro de Investigacion en Matematicas (CIMAT), Guanajuato, Mexico, in 2007, and the Ph.D. degree in electronics engineering with UASLP, in 2015, with a focus on numerical methods for characterization of living tissue using time-resolved fluorescence lifetime imaging microscopy data. Since 2015, he has been a Full Professor with the Universidad Autónoma de Aguascalientes. His research interests include numerical programming, machine learning, and multi/hiper-spectral imaging applications in food science and clinical diagnosis.

JOSE J. RICO-JIMENEZ received the B.S. degree in computer engineering from Universidad Lasallista Benavente, Celaya, Mexico, the M.S. degree in computer engineering from the Instituto Politecnico Nacional campus CICATA-QRO, Queretaro, Mexico, and the Ph.D. degree in biomedical engineering from Texas A&M University, College Station, TX, USA. From February 2017 to July 2018, he was a Postdoctoral Research Fellow with the Beckman Institute, University of Illinois at Urbana–Champaign. Since July 2018, he holds a Postdoctoral Research Fellow position with Texas A&M University. His research areas of interest are biomedical imaging, data analysis and visualization. He is also focusing on biomedical imaging applications for atherosclerosis and oral cancer using fluorescence lifetime imaging (FLIM), optical coherence tomography (OCT), and OCT angiography.

ELVIS DURAN-SIERRA received the B.Sc. degree in mechatronics engineering from Anahuac Mayab University, Merida, Yucatan, Mexico, in 2012. He is currently pursuing the Ph.D. degree in biomedical engineering with Texas A&M University (TAMU), College Station, TX, USA. In 2012, he started to work as a Software Engineer with Plenumsoft, where he developed machine learning algorithms for the classification of hyperspectral and satellite images. In 2015, he began conducting research with the Optical Diagnosis and Imaging Laboratory, TAMU, under the supervision of Dr. J. Jo, where he developed algorithms for FLIM image processing, statistical analysis, and classification. His research activity conducted at TAMU focuses on the development of computational algorithms for the automated, non-invasive, and in situ detection of oral cancer in patients based on fluorescence lifetime imaging (FLIM) endoscopy. His research interests include software development, medical imaging, statistical analysis, and machine learning for the automated clinical diagnosis of high-risk diseases in patients, such as oral cancer.

HIMAR FABELO received the Telecommunication Engineering and the M.Sc. and Ph.D. degrees in telecommunication technologies from the University of Las Palmas de Gran Canaria (ULPGC), Las Palmas de Gran Canaria, Spain, in 2013, 2014, and 2019, respectively. Since then, he has conducted his research activity with the Integrated System Design Division, Institute for Applied Microelectronics (IUMA), University of Las Palmas de Gran Canaria, in the field of electronic and bioengineering. In 2015, he started to work as a Coordination Assistant and RESearcher with the HELICoiD European Project, co-funded by the European Commission. In 2018, he performs a research stay with the Department of Bioengineering, Erik Jonsson School of Engineering and Computer Science, The University of Texas at Dallas (UTD), collaborating with Prof. B. Fei in the field of medical hyperspectral imaging analysis using deep learning. His research interest area include the use of machine learning and deep learning techniques applied to hyperspectral images to discriminate between healthy and tumor samples for human–brain tissues in real-time during neurosurgical operations.

SAMUEL ORTEGA received the degree in telecommunication engineering and the M.Sc. degree in telecommunication technologies from the University of Las Palmas de Gran Canaria (ULPGC), Spain, in 2014 and 2015, respectively. Since then, he has conducted his research activity in the Integrated System Design Division with the Institute for Applied Microelectronics (IUMA), University of Las Palmas de Gran Canaria, in the field of electronic and bioengineering. In 2015, he started to work as a Coordination Assistant and a Researcher with the HELICoiD European Project, co-funded by the European Commission. His current research interests are in the use of machine learning algorithms in medical applications using hyperspectral images.

GUSTAVO CALLICÓ (M'08) received the M.S. degree in telecommunication engineering, the Ph.D. degree, and the European Doctorate degree (Hons.) from the University of Las Palmas de Gran Canaria (ULPGC), in 1995 and 2003, respectively. From 1996 to 1997, he was granted with a research grant from the National Educational Ministry and hired by the University as an Electronic Lecturer, in 1997. In 1994, he joined the Institute for Applied Microelectronics (IUMA). From 2000 to 2001, he stayed at the Philips Research Laboratories (NatLab), Eindhoven, The Netherlands, as a Visiting Scientist, where he developed his Ph.D. thesis. He currently develops his research activities in the Integrated Systems Design Division, Institute for Applied Microelectronics (IUMA). He is currently an Associate Professor with ULPGC. He has more than 170 publications in national and international journals, conferences, and book chapters. He has participated in 18 research projects funded by the European Community, the Spanish Government and international private industries. He has been an Associate Editor of the IEEE Transactions on Consumer Electronics, in 2009. He is currently a Senior Associate Editor of the IEEE Transactions on Consumer Electronics. Additionally, he is an Associate Editor of the IEEE Access, in 2016. Since 2015, he has been responsible for the scientific-technological equipment project called "Hyperspectral image acquisition system of high spatial and spectral definition", granted by the General Directorate of Research and Management of the National Research and Development Plan, funded through the General Directorate of Scientific Infrastructure. He has been the coordinator of the European project HELICoiD (FET, Future and Emerging Technologies) under the Seventh Framework Program with Grant Agreement 618080. He has been an invited professor with the University of Pavia, Italy, in October 2015 and March 2019. His current research fields include hyperspectral imaging for real-time cancer detection (brain, skin, and cervix), real-time super-resolution algorithms, synthesis-based design for SOCs, and circuits for multimedia processing and video coding standards, especially for H.264 and SVC.

JAVIER A. JO received the B.S. degree in electrical engineering from the Pontificia Universidad Católica del Perú, in 1996, and the M.S. degree in electrical engineering (signal and image processing) and the Ph.D. degree in biomedical engineering (physiological mathematical modeling) from the University of Southern California, Los Angeles, in 2000 and 2002, respectively. In 2002, he changes his research focus to the field of biophotonics and has continued working in this field since then. Prior to starting his academic appointments, he was a Postdoctoral Fellow within the Department of Surgery, Cedars-Sinai Medical Center, Los Angeles from 2002 to 2005, and a Project Scientist within the Department of Biomedical Engineering, University of California at Davis, Davis, in 2006. In 2006, he joined the Faculty of the Department of Biomedical Engineering, Texas A&M University, where he established the Laboratory for Optical Diagnosis and Imaging (LODI). In 2019, he joined the Faculty of the School of Electrical and Computer Engineering, The University of Oklahoma. The overall mission of his research program is to develop optical sensing and imaging technologies that will impact how we study pathophysiological mechanism underlying major human diseases and clinically manage patients suffering from these diseases. While most academic labs in the field of biomedical imaging focus on either instrumentation development or computational imaging science, he leads a very unique research program dedicated to address major unmet needs in both biomedical research and clinical practice through the design, development, and validation of both optical spectroscopy/imaging instrumentation and computational tools and methods for the nondestructive, non or minimally invasive morphological, and molecular and physiological characterization of biological and engineered tissues at multiple spatial and temporal scales.